

Cite this: *Chem. Sci.*, 2018, 9, 1375

# Extraction of nickel from NiFe-LDH into Ni<sub>2</sub>P@NiFe hydroxide as a bifunctional electrocatalyst for efficient overall water splitting†

Fang-Shuai Zhang,<sup>‡a</sup> Jia-Wei Wang,<sup>‡a</sup> Jun Luo,<sup>b</sup> Rui-Rui Liu,<sup>b</sup> Zhi-Ming Zhang,<sup>‡b</sup> Chun-Ting He<sup>\*a</sup> and Tong-Bu Lu<sup>‡ab</sup>

The development of highly efficient, low-cost and stable electrocatalysts for overall water splitting is highly desirable for the storage of intermittent solar energy and wind energy sources. Herein, we show for the first time that nickel can be extracted from NiFe-layered double hydroxide (NiFe-LDH) to generate an Ni<sub>2</sub>P@FePO<sub>x</sub> heterostructure. The Ni<sub>2</sub>P@FePO<sub>x</sub> heterostructure was converted to an Ni<sub>2</sub>P@NiFe hydroxide heterostructure (P-NiFe) during water splitting, which displays high electrocatalytic performance for both the hydrogen evolution reaction (HER) and oxygen evolution reaction (OER) in 1.0 M KOH solution, with an overpotential of 75 mV at 10 mA cm<sup>-2</sup> for HER, and overpotentials of 205, 230 and 430 mV at 10, 100 and 1000 mA cm<sup>-2</sup> for OER, respectively. Moreover, it could afford a stable current density of 10 mA cm<sup>-2</sup> for overall water splitting at 1.51 V in 1.0 M KOH with long-term durability (100 h). This cell voltage is among the best reported values for bifunctional electrocatalysts. The results of theoretical calculations demonstrate that P-NiFe displays optimized adsorption energies for both HER and OER intermediates at the nickel active sites, thus dramatically enhancing its electrocatalytic activity.

Received 23rd October 2017  
Accepted 21st December 2017

DOI: 10.1039/c7sc04569g

rsc.li/chemical-science

## Introduction

To address energy and environmental problems, hydrogen fuel has been regarded as a promising alternative to fossil fuels for its high energy density and cleanness.<sup>1</sup> Electrochemical water splitting has been regarded as a promising method for the production of hydrogen, using electric energy coming from intermittent solar energy and wind energy sources.<sup>2</sup> However, water splitting is a thermodynamically uphill process, accompanied by high overpotentials ( $\eta$ ) for both HER and OER, which requires efficient and stable electrocatalysts to significantly reduce the overpotentials.<sup>3</sup> As is well known, Pt-based materials and iridium oxides are the state-of-the-art electrocatalysts for HER and OER, respectively,<sup>4</sup> while their high cost and scarcity seriously limit their large-scale application. Therefore, there has been growing interest in developing earth-abundant and cheap electrocatalysts for water splitting, and great progress has been achieved over past years. It has been found that transition-metal sulfides,<sup>5</sup> carbides,<sup>6</sup> selenides<sup>7</sup> and phosphides<sup>8</sup> can

dramatically reduce the overpotentials for HER in acidic media, and the transition-metal oxides/hydroxides<sup>9</sup> exhibit remarkable electrocatalytic activity for OER in alkaline solution. However, it remains a great challenge to pair the HER and OER electrocatalysts in an integrated electrolyzer for efficient overall water splitting, due to the mismatch between their best working conditions. Bifunctional electrocatalysts to facilitate both HER and OER in the same electrolyte are highly appealing, as this can lower the total cost by avoiding the preparation of different catalysts, and make water splitting feasible for practical use.<sup>3b,4a,10</sup> Nonetheless, only a few bifunctional electrocatalysts display competitive catalytic activity to that of a Pt-IrO<sub>x</sub>-coupled electrolyzer that can reduce the overall water splitting cell voltage to near 1.5 V at a current density of 10<sup>3b,4a,10c</sup> or 20 mA cm<sup>-2</sup>.<sup>10e</sup> In this context, the design and synthesis of efficient bifunctional electrocatalysts for overall water splitting in the same electrolyte still remain a great challenge.

Previous studies have revealed that binary/ternary metal hydroxides/oxides exhibit higher electrocatalytic performance for OER than their unary counterparts,<sup>11</sup> possibly due to the optimized binding energies for OER intermediates (\*OH, \*O, and \*OOH) on the catalyst surface,<sup>9c</sup> and/or enhanced charge transferability of the catalysts in the presence of doping elements. NiFe-layered double hydroxide (NiFe-LDH) based nanomaterials, with binary metal centers evenly mixed on a molecular level, have shown high performance on OER, with low overpotentials of 210–350 mV at 10 mA cm<sup>-2</sup>.<sup>9a,10e,12</sup> However, when they were used as a bifunctional electrocatalyst

<sup>a</sup>MOE Key Laboratory of Bioinorganic and Synthetic Chemistry, School of Chemistry, Sun Yat-Sen University, Guangzhou 510275, China. E-mail: hechunt@mail2.sysu.edu.cn; lutongbu@mail.sysu.edu.cn

<sup>b</sup>Institute of New Energy Materials & Low Carbon Technology, School of Material Science & Engineering, Tianjin University of Technology, Tianjin 300384, China. E-mail: zmzhang@email.tjut.edu.cn

† Electronic supplementary information (ESI) available: Experimental and computational details and additional data. See DOI: 10.1039/c7sc04569g

‡ F. S. Zhang and J. W. Wang contributed equally to this work.

for overall water splitting, the cell voltage was as high as 1.7 V at a current density of  $10 \text{ mA cm}^{-2}$  in 1.0 M KOH,<sup>12b</sup> due to their higher overpotential for HER. Accordingly, decreasing the overpotential for HER will make NiFe-LDH into an efficient bifunctional electrocatalyst for overall water splitting.

Recently, transition-metal phosphides have also been demonstrated as efficient electrocatalysts for HER in an alkaline medium,<sup>8h,8i,13</sup> besides their high HER catalytic activity in acidic media.<sup>8a,8d,8g,14</sup> In addition, it has been demonstrated that bimetallic phosphide NiCoP displays higher HER activity than monometallic phosphide Ni<sub>2</sub>P, due to its optimized H binding energy of nearly zero (close to that of Pt) on the surface of NiCoP, which is beneficial for the reversible adsorption and desorption of H.<sup>13a</sup> We presume that the HER activity could be improved by the phosphorization of NiFe-LDH to get a bimetallic phosphide NiFeP, and combine it with a highly efficient NiFe-LDH OER electrocatalyst to construct a NiFeP/NiFe-LDH-coupled electrolyzer, when the cell voltage would be dramatically decreased. Unexpectedly, an Ni<sub>2</sub>P@FePO<sub>x</sub> heterostructure was obtained during the phosphorization of NiFe-LDH, in which Ni was selectively phosphorized and extracted from NiFe-LDH. Ni<sub>2</sub>P@FePO<sub>x</sub> further evolved to Ni<sub>2</sub>P@NiFe hydroxide (P-NiFe) during water splitting, which shows a much lower overpotential of 75 mV than that of 230 mV for NiFe-LDH at  $10 \text{ mA cm}^{-2}$  for HER in 1.0 M KOH solution. More interestingly, P-NiFe also shows a better OER performance than NiFe-LDH in 1.0 M KOH solution, with overpotentials of 205, 230 and 430 mV at current densities of 10, 100 and 1000  $\text{mA cm}^{-2}$ , respectively, much lower than the corresponding values of 250, 280, and 560 mV for NiFe-LDH at current densities of 10, 100 and 1000  $\text{mA cm}^{-2}$ , respectively. Therefore, a P-NiFe heterostructure can serve as an efficient bifunctional electrocatalyst for an alkaline electrolyzer, generating a cell voltage of only 1.51 V at  $10 \text{ mA cm}^{-2}$  in 1.0 M KOH solution, even better than the combination of the state-of-the-art IrO<sub>2</sub> and Pt/C as benchmark electrocatalysts. Though a number of NiFe-based metal hydroxides/oxides<sup>9a,12b-f,12h</sup> and transition-metal phosphides<sup>8a,8e,8f,8i,15</sup> have been reported as electrocatalysts for OER and HER, to our knowledge, the selective extraction and phosphorization of a single metal from mixed metal hydroxides/oxides to form a heterostructure has not been documented so far. The *in situ* transformed Ni<sub>2</sub>P@NiFe hydroxide heterostructure not only enhances its conductivity due to the existence of metallic Ni<sub>2</sub>P, but also optimizes the adsorption energies for both HER and OER intermediates at the nickel active sites on its surface, thus dramatically enhancing its electrocatalytic activity for both OER and HER.

## Experimental section

### Materials

Ni(NO<sub>3</sub>)<sub>2</sub>·6H<sub>2</sub>O (99.9985% metals basis, Alfa), Fe(NO<sub>3</sub>)<sub>3</sub>·9H<sub>2</sub>O (98+% metals basis, Alfa), urea (99.999%, Aladdin), NaH<sub>2</sub>PO<sub>2</sub> (99.0%, Aladdin), IrO<sub>2</sub> (99.99% metals basis, Alfa), 20% Pt on Vulcan XC72 (20% Pt/C, Sigma-Aldrich), Nafion (5 wt%, Sigma-Aldrich), nickel foam (>99.5%, 1.0 mm thick, Taiyuan Yingze Lizhiyuan Battery) and other materials were obtained from

commercial suppliers and used without further purification, unless otherwise noted.

### Characterization

Scanning electron microscopy (SEM) and energy dispersive X-ray spectroscopy (EDS) results were collected by a field emission scanning electron microscope (FEI, Quanta 400). High-resolution transmission electron microscope (HRTEM) images, quantitative EDS data and electron energy loss spectroscopy (EELS) elemental mapping were taken on an aberration-corrected scanning transmission electron microscope (STEM, FEI Titan Cubed Themis G2 300 at 200 and 300 kV). The powder X-ray diffraction measurements were performed on a D8 ADVANCE X-ray Diffractometer. The X-ray photoelectron spectroscopy (XPS) data was collected on an ESCA Lab250 instrument. Raman spectra were carried out on a Renishaw in Via Laser Micro-Raman Spectrometer (Horiba-Jobin-Yvon T64000 instrument) using a 514 nm laser. Electrocatalytic properties were studied with a standard three-electrode system controlled by a CHI760E electrochemical workstation. An Ag/AgCl (in 3 M KCl solution) electrode and a carbon rod were used as the reference electrode and the counter electrode, respectively. The linear sweep voltammetry curves were recorded at a scan rate of  $5 \text{ mV s}^{-1}$  in 1.0 M KOH solution. The electrochemical impedance spectroscopy (EIS) measurements were conducted over a frequency range from 10 kHz to 100 kHz. The analysis of the gas product was operated on a gas chromatograph (Agilent 7820A-GC, molecular sieve columns, thermal-conductivity detector, TCD).

### Preparation

**Preparation of NiFe-LDH@NF.** The NiFe-LDH was prepared according to a modified literature method.<sup>12b</sup> Ni(NO<sub>3</sub>)<sub>2</sub>·6H<sub>2</sub>O (0.5 mmol), Fe(NO<sub>3</sub>)<sub>3</sub>·9H<sub>2</sub>O (0.5 mmol) and urea (2.5 mmol) were mixed in 40 mL of deionized water. The resulting solution was poured into a 50 mL autoclave with a piece of  $1 \times 2 \text{ cm}$  NF leaning against the wall. The growth was carried out at 120 °C in an electric oven for 12 h. After natural cooling to room temperature, the NiFe-LDH sample coated on NF was collected, washed with deionized water, and then blown dry under a stream of compressed air.

**Preparation of Ni(OH)<sub>2</sub>@NF.** Ni(OH)<sub>2</sub>@NF was prepared by a similar procedure to the synthesis of NiFe-LDH@NF without adding Fe(NO<sub>3</sub>)<sub>3</sub>·9H<sub>2</sub>O, and 1 mmol Ni(NO<sub>3</sub>)<sub>2</sub>·6H<sub>2</sub>O was used in the synthesis process.

**Preparation of P-NiFe@NF and P-Ni@NF.** 250 mg of NaH<sub>2</sub>PO<sub>2</sub> was placed at the upstream side of a tube furnace and one piece of  $1 \times 2 \text{ cm}$  NiFe-LDH@NF was located at the downstream side of the furnace. Then, the furnace was heated to 573 K with a heating rate of  $2 \text{ K min}^{-1}$  under an Ar flow, and maintained at 573 K for 3 h. After natural cooling to room temperature, Ni<sub>2</sub>P@FePO<sub>x</sub> was obtained, which was *in situ* transformed to Ni<sub>2</sub>P@NiFe hydroxide (P-NiFe@NF electrode) during water splitting. The Ni<sub>2</sub>P@Ni(OH)<sub>2</sub> (P-Ni@NF) was prepared by a similar procedure with P-NiFe/NF using Ni(OH)<sub>2</sub>@NF instead of NiFe-LDH@NF. The amount of



$\text{Ni}_2\text{P}@/\text{FePO}_x$  or  $\text{Ni}_2\text{P}$  loading on NF, which was determined by the weight difference of NF before and after material growth, is approximately  $1.0 \text{ mg cm}^{-2}$ .

**Preparation of 20%  $\text{Pt}/\text{C}@/\text{NF}$  and  $\text{IrO}_2@/\text{NF}$ .** 10 mg of 20%  $\text{Pt}/\text{C}$  (or  $\text{IrO}_2$ ) and 50  $\mu\text{L}$  of Nafion (5 wt%) were dispersed in 1 mL of ethanol with sonication for at least 30 min to generate a homogeneous ink. Then 150  $\mu\text{L}$  of the ink was drop-casted onto a NF, and the solvent was evaporated at room temperature overnight. The amount of loading is approximately  $1.0 \text{ mg cm}^{-2}$ .

### Estimation of effective electro-chemical surface area (ECSA)

To evaluate the ECSA, cyclic voltammetry (CV) was carried out to probe the electrochemical double-layer capacitance ( $C_{\text{dl}}$ ) of various samples in the non-faradaic region from CV in a quiescent solution. This non-faradaic region is typically a 0.1 V window with the open circuit potential as the middle point. All measured current in this region is assumed to be due to double-layer charging. By plotting the current density at 0.92 V vs. RHE against the scan rate, a linear trend was observed. The linear slope, equivalent to twice of the double-layer capacitance  $C_{\text{dl}}$ , was used to represent the ECSA.

### Estimation of Faraday efficiency

The detection of hydrogen and oxygen was performed in a one-compartment, two-electrode cell with stirring. Two P-NiFe@NF electrodes ( $1 \times 1 \text{ cm}$ ) were used as the working electrode and the counter electrode, respectively. Before the detection of the gas product, the cell was firmly sealed to be gas-tight and subsequently purged with argon for 20 min. Before and after the electrolysis at a current density of  $10 \text{ mA cm}^{-2}$ , the gas products were analyzed by gas chromatography.

### DFT calculation

According to previous studies,<sup>16</sup> the Gibbs free energy of each elementary step of OER or HER were calculated as follows:

$$\Delta G = \Delta E + \Delta \text{ZPE} - T\Delta S$$

where  $\Delta E$  is the reaction energy calculated by using the spin polarization density functional theory (DFT) method.  $\Delta \text{ZPE}$  and  $\Delta S$  are the changes in zero point energies and entropy during the reaction, respectively. In the case of HER calculations, as the vibrational entropy of  $\text{H}^*$  in the adsorbed state is small, the entropy of adsorption of  $1/2\text{H}_2$  is  $\Delta S_{\text{H}} \approx -0.5S_{\text{OH}_2}$ , where  $S_{\text{OH}_2}$  is the entropy of  $\text{H}_2$  in the gas phase under the standard conditions. Therefore the overall corrections were taken as in<sup>17</sup>

$$\Delta G_{\text{H}^*} = \Delta E_{\text{H}^*} + 0.24 \text{ eV}$$

Based on the structural characterizations, the periodical surface models of the heterostructures were constructed by using the crystal structures of  $\text{Ni}_2\text{P}$  (inner layer) and  $\text{Ni}/\text{Fe}$  hydroxide (outer layer), and the latter were all set to be charge neutral by tuning the numbers of H atoms on the oxygen. The

higher index  $(1\bar{1}\bar{2})$  facet of  $\text{Fe}/\text{Ni}(\text{OH})_x$ , containing under-coordinated metal sites similar to a step or edge, was adopted as it possesses higher OER activity.<sup>18</sup> A vacuum slab of 15 Å is used to separate the layer from its periodic images. All the geometrical optimizations and energy calculations were performed by the Dmol<sup>3</sup> module in Materials Studio 5.5. The widely used generalized gradient approximation (GGA) with the Perdew–Burke–Ernzerhof (PBE) function and the double numerical plus polarization (DNP) basis set were used for all the non-metal atoms. An accurate DFT semi-core pseudopotentials (DSPP) was employed for metal atoms, and thermal smearing was applied to the orbital occupation to speed up convergence. For all the DFT calculations, the energy, gradient and displacement convergence criteria were set at  $2 \times 10^{-5} \text{ Ha}$ ,  $4 \times 10^{-3} \text{ Å}$  and  $5 \times 10^{-3} \text{ Å}$ , respectively.

## Results and discussion

### Synthesis and characterization

The  $\text{Ni}_2\text{P}@/\text{FePO}_x$  heterostructure was prepared by the phosphorization of highly dense, vertically aligned NiFe-LDH nanosheets on an NF (nickel foam) substrate (Scheme 1). At first, the vertically aligned NiFe-LDH nanosheets were uniformly grown on the NF substrate by a hydrothermal method, as observed by SEM (Fig. S1†), and its phase purity was confirmed by the X-ray diffraction (XRD) measurement (Fig. S2†). Subsequently, the NiFe-LDH nanosheets were phosphorized using  $\text{NaH}_2\text{PO}_2$  as a P source. With plenty of parallel experiments, it was found that the phosphorization temperature plays a key role during the formation of  $\text{Ni}_2\text{P}@/\text{FePO}_x$  nanosheets. Based on the decomposition temperature of  $\text{NaH}_2\text{PO}_2$  (above 473 K),<sup>19</sup> the phosphorization temperatures were selected from 473 to 773 K, with a controlled reaction time scale of 3 h. As shown in Fig. S3a,† the morphology of the sample prepared at 473 K barely changed compared to that of the original NiFe-LDH nanosheets, and a large amount of  $\text{NaH}_2\text{PO}_2$  was found to be unreacted, suggesting that the phosphorization temperature of 473 K is too low. The nanosheet-like morphology of the sample obtained at 573 K can be retained, though the sheet edges become thicker compared to those of the original NiFe-LDH nanosheets (Fig. S3b†). Further increasing the phosphorization temperatures to 673 and 773 K will destroy the morphology of the nanosheets



Scheme 1 The procedure for the synthesis of  $\text{Ni}_2\text{P}@/\text{FePO}_x$  nanosheets.





(Fig. S3c and d†). On the other hand, the phosphorization time was also found to play an important role during the formation of  $\text{Ni}_2\text{P}@FePO_x$  nanosheets, and 3 h was found to be an ideal phosphorization time for the preparation of  $\text{Ni}_2\text{P}@FePO_x$  nanosheets (Fig. S4b†). Further increasing the phosphorization time will destroy the morphology of the nanosheets (Fig. S4c†). Therefore, the optimized phosphorization temperature and time are 573 K and 3 h, respectively, and the  $\text{Ni}_2\text{P}@FePO_x$  nanosheets synthesized under such optimized conditions were used as an electrocatalyst for further investigation (see Scheme 1). The direct integration of an  $\text{Ni}_2\text{P}@FePO_x$  electrocatalyst on NF not only provides conductive support and a 3D macroporous feature which can be used directly as an electrode, but also avoids the use of expensive electrodes and the requirement for extra glues to stick the catalysts onto the surface of such electrodes, which is beneficial for a commercial water electrolyzer.

X-ray photoelectron spectroscopy (XPS) was used to determine the chemical composition on the surface of  $\text{Ni}_2\text{P}@FePO_x$ . As shown in Fig. 1a, the XPS of as-prepared  $\text{Ni}_2\text{P}@FePO_x$  material exhibits a binding energy peak at 853.5 eV, and this peak is absent in the XPS pattern of NiFe-LDH, which can be attributed to metallic nickel in the nickel phosphide ( $\text{Ni}_2\text{P}$ ).<sup>15b</sup> The presence of  $\text{Ni}_2\text{P}$  in the  $\text{Ni}_2\text{P}@FePO_x$  sample can be further confirmed by the X-ray diffraction (XRD) measurements, which show the characteristic diffraction peaks of  $\text{Ni}_2\text{P}$  (Fig. S5†). The XPS patterns also display the binding energies of Ni  $2p_{3/2}$  and Ni  $2p_{1/2}$  peaks located at 857.2 and 875.2 eV, respectively (Fig. 1a). These values are in good agreement with those of  $\text{Ni}^{2+}$  in NiFe-LDH and other nickel oxides or phosphates,<sup>8f,15a</sup> which can be attributed to the surface oxidation of  $\text{Ni}_2\text{P}$ . The peaks of Fe  $2p_{3/2}$  and Fe  $2p_{1/2}$  in the P-NiFe sample appear at 712.5 and 725.5 eV, respectively (Fig. 1b), demonstrating the presence of the  $\text{Fe}^{3+}$  state.<sup>14</sup> In addition, the XPS pattern of P 2p shows the existence of both metal phosphide (129.7 eV)<sup>8e,15c</sup> and metal phosphate (134.3 eV, Fig. 1c).<sup>13b,15c</sup> The binding energy of 853.5 eV is slightly higher than that of metallic Ni (852.6 eV),<sup>20</sup> while the binding energy of 129.7 eV is slightly lower than that of elemental P (130.0 eV),<sup>20</sup> indicating that the Ni and P are partially positive and negatively charged in  $\text{Ni}_2\text{P}$ , respectively. All the above results indicate the co-existence of  $\text{Ni}_2\text{P}$ ,  $\text{Ni}^{2+}$ ,  $\text{Fe}^{3+}$  and metal phosphate species in the  $\text{Ni}_2\text{P}@FePO_x$  sample.

To further analyze the morphology and composition of the as-prepared  $\text{Ni}_2\text{P}@FePO_x$  sample, a scanning transmission electron microscope (STEM) with a high-angle annular dark field (HAADF) mode was utilized. As shown in Fig. 2a and S6,†



Fig. 2 (a) TEM image, (b) HRTEM image, (c) HAADF-STEM image and EDS elemental mapping images for the  $\text{Ni}_2\text{P}@FePO_x$  sample.

the high-resolution transmission electron microscope (HRTEM) images show crystalline nanoparticles (10–20 nm) embedded in an amorphous substrate. The lattice fringes of the crystalline nanoparticles can be clearly observed (Fig. 2b), where the (200) crystal facet with a  $d$ -spacing of 0.197 nm is in agreement with the crystal phase of  $\text{Ni}_2\text{P}$  (JCPDS no. 74-1385), further demonstrating the formation of crystalline  $\text{Ni}_2\text{P}$  nanoparticles in  $\text{Ni}_2\text{P}@FePO_x$ . In the substrate, no lattice fringes can be observed, suggesting the amorphous nature of the substrate. As shown in the energy dispersive X-ray spectroscopy (EDS) elemental mapping images (Fig. 2c), the majority of the Ni element is distributed in the crystalline  $\text{Ni}_2\text{P}$  nanoparticles, while the Fe and O elements are mainly dispersed in the amorphous substrate. Additionally, the P element is distributed over the  $\text{Ni}_2\text{P}@FePO_x$  sample homogeneously. These observations indicate that the crystalline nanoparticles are mainly comprised of  $\text{Ni}_2\text{P}$ , and the amorphous substrate is most likely to be iron phosphate ( $FePO_x$ ). The presence of  $Fe_2O_3$  species in the amorphous substrate can be excluded by comparison of the results of electron energy loss spectroscopy (EELS) for P-NiFe with those of the  $Fe_2O_3$  sample (Fig. S7†).<sup>21</sup> The results of EDS measurement for the  $\text{Ni}_2\text{P}@FePO_x$  sample reveal that the ratio of Ni : P : Fe : O is approximately 2 : 2 : 1 : 4 (Fig. S8†), indicating that the ratio of  $\text{Ni}_2\text{P}$  and  $FePO_x$  ( $x \approx 4$ )<sup>22</sup> in  $\text{Ni}_2\text{P}@FePO_x$  is approximately 1 : 1. All the above observations clearly demonstrate that the  $\text{Ni}_2\text{P}@FePO_x$  sample consists of crystalline  $\text{Ni}_2\text{P}$  nanoparticles embedded in amorphous iron phosphate, forming an  $\text{Ni}_2\text{P}@FePO_x$  heterostructure. The formation of  $\text{Ni}_2\text{P}$  nanoparticles suggests that Ni was selectively



Fig. 1 The XPS patterns of as-prepared  $\text{Ni}_2\text{P}@FePO_x$  sample, showing the signals of (a) Ni 2p, (b) Fe 2p and (c) P 2p.

phosphorized and extracted from NiFe-LDH during the phosphorization process. This is possibly because the  $\text{Ni}^{2+}$  in NiO and  $\text{Ni}(\text{OH})_2$  could be easily phosphorized to form  $\text{Ni}_2\text{P}$  by substantial substitution of O atoms by P atoms.<sup>8f</sup> In contrast, the iron hydroxide was transformed to iron phosphate rather than iron phosphide, presumably due to the high affinity of  $\text{Fe}^{3+}$  towards O, which may hinder the substitution of O atoms by P atoms.<sup>21</sup> The extraction of Ni from NiFe-LDH during the phosphorization process will produce a large amount of defects in the synthesized  $\text{Ni}_2\text{P}@/\text{FePO}_x$  heterostructure, which will provide more active sites for HER and OER, giving rise to enhanced HER and OER activity.

### Electrocatalytic HER

The electrocatalytic activity of as-prepared  $\text{Ni}_2\text{P}@/\text{FePO}_x$  for HER was investigated in 1.0 M KOH aqueous solution, and the results indicate that  $\text{Ni}_2\text{P}@/\text{FePO}_x$  was converted to  $\text{Ni}_2\text{P}@/\text{NiFe}$  hydroxide (P-NiFe) during HER as a real electrocatalyst (see below). For comparison, the electrocatalytic performances of NiFe-LDH, P-Ni (obtained by phosphorization of nickel hydroxides) and commercial 20% Pt/C coated on NF were also investigated under the same conditions. It is exciting to note that P-NiFe exhibits high catalytic activity for HER in alkaline aqueous solution, with an overpotential of 75 mV at  $10 \text{ mA cm}^{-2}$  (Fig. 3a). This value is much lower than those of P-Ni (190 mV) and NiFe-LDH (230 mV) under the same conditions, and is comparable to that of commercial 20% Pt/C (45 mV). Moreover, the Tafel slope of P-NiFe ( $67 \text{ mV dec}^{-1}$ ) is also lower than those of P-Ni ( $107 \text{ mV dec}^{-1}$ ) and NiFe-LDH ( $264 \text{ mV dec}^{-1}$ ; Fig. 3b), indicating the rapid HER catalytic rate of P-NiFe. Besides the high catalytic efficiency for HER, the P-NiFe catalyst also exhibits impressive robustness during a 25 h controlled-current

electrolysis (CCE) at  $10 \text{ mA cm}^{-2}$ , with a stable overpotential of 75 mV (Fig. 3c). Meanwhile, the LSV curves before and after 25 h of CCE further confirm its high stability during the HER (Fig. 3d). The bare NF shows poorer activity for HER than that of P-NiFe under identical conditions (Fig. S9a†).

After the CCE for HER at  $10 \text{ mA cm}^{-2}$  for 25 h, HRTEM (Fig. S10†) and elemental mapping images (Fig. S11†) of the generated sample indicate that there was no obvious change in the morphology of the crystalline  $\text{Ni}_2\text{P}$  nanoparticles, while the amorphous iron phosphate was transformed to crystalline  $\text{Fe}(\text{OH})_3$  in 1.0 M KOH, and this was confirmed by XRD measurement (Fig. S12†), which demonstrates that both crystalline  $\text{Ni}_2\text{P}$  and  $\text{Fe}(\text{OH})_3$  coexist in P-NiFe after the CCE for HER. However, the low-energy peaks of 853.5 and 129.7 eV belonging to  $\text{Ni}_2\text{P}$  disappeared in the XPS patterns for the P-NiFe sample after CCE (Fig. S13†), and only the peaks (857.1 and 875.2 eV) attributed to  $\text{Ni}^{2+}$  were observed, indicating that the surface of  $\text{Ni}_2\text{P}$  was oxidized into  $\text{Ni}(\text{OH})_2$  in alkaline solution, and the  $\text{Ni}(\text{OH})_2$  formed *in situ* at the surface of the  $\text{Ni}_2\text{P}$  nanoparticles prevents further oxidation of  $\text{Ni}_2\text{P}$ . However, the peak of 133.2 eV belonging to P 2p can be observed (Fig. S13c†), indicating that the  $\text{Ni}(\text{OH})_2$  layer formed *in situ* at the surface of the  $\text{Ni}_2\text{P}$  is very thin. The XPS patterns for the P-NiFe sample after the LSV measurement and before CCE (Fig. S14†) is similar to those after CCE, indicating that the surface oxidation of  $\text{Ni}_2\text{P}$  into  $\text{Ni}(\text{OH})_2$  occurs rapidly in solution. The surface oxidation of  $\text{Ni}_2\text{P}$  into  $\text{Ni}(\text{OH})_2$  and the transformation of amorphous iron phosphate into  $\text{Fe}(\text{OH})_3$  in  $\text{Ni}_2\text{P}@/\text{FePO}_x$  after CCE were further confirmed by the results of Raman spectra measurements (Fig. S15†), which show very weak characteristic peaks of NiFe hydroxide, indicating the presence of trace amounts of NiFe hydroxide on the surface of the  $\text{Ni}_2\text{P}$  nanoparticles.<sup>13c,23</sup> The results of electrochemical impedance spectroscopy (EIS) measurements indicate that the conductivity of P-NiFe after HER is dramatically increased compared to that of NiFe-LDH after HER (Fig. S16a†), which can be attributed to the existence of highly conductive metallic  $\text{Ni}_2\text{P}$  nanoparticles in P-NiFe. The results of effective electro-chemical surface area (ECSA) measurements (Fig. S17a†) indicate that number of active sites in P-NiFe after CCE for HER ( $29.1 \text{ mF cm}^{-2}$ ) is 17-fold higher than those of NiFe-LDH after CCE for HER ( $1.7 \text{ mF cm}^{-2}$ ). The increased number of active sites in P-NiFe could be ascribed to the extraction of Ni from NiFe-LDH during the phosphorization process, which generates a large amount of defects to act as catalytically active sites. Indeed, the surface of P-NiFe after HER becomes rougher compared with that of as-synthesized  $\text{Ni}_2\text{P}@/\text{FePO}_x$  (Fig. S18†), indicating that more active sites were exposed.

To reveal the origin of the enhanced HER activity of the P-NiFe, density functional theory (DFT) calculations were carried out. Generally, hydrogen evolution activity is closely related with the Gibbs free energy of hydrogen adsorption ( $\Delta G_{\text{H}^*}$ ) on the surfaces of catalysts in both acid and alkaline conditions, so  $|\Delta G_{\text{H}^*}|$  is one of the key catalytic descriptors for theoretical prediction of HER activity, which is usually proposed as having an optimal value close to zero.<sup>24</sup> In this context, we investigated seven model structures by the calculation of the



Fig. 3 (a) IR-corrected linear sweep voltammetry (LSV) curves, with a scan rate of  $5 \text{ mV s}^{-1}$ . (b) Tafel plots and (c) current density traces of CCE at  $10 \text{ mA cm}^{-2}$  for HER in 1.0 M KOH. (d) LSV curves for P-NiFe before (black line) and after (red line) CCE for HER at  $10 \text{ mA cm}^{-2}$  for 25 h. Catalysts: P-NiFe (black), NiFe-LDH (red), P-Ni (blue) and 20% Pt/C (green).



free energies for H adsorption on the surfaces of different catalytic sites of  $\text{Ni}_2\text{P}$ ,  $\text{Ni}(\text{OH})_2$ ,  $\text{FeO}(\text{OH})$ ,  $\text{Ni}_2\text{P}@\text{Ni}(\text{OH})_2$ ,  $\text{Ni}_2\text{-P}@\text{FeO}(\text{OH})$ ,  $\text{NiFeO}(\text{OH})_3$  (corresponding to NiFe-LDH), and  $\text{Ni}_2\text{P}@\text{NiFeO}(\text{OH})_3$  (corresponding to P-NiFe) (Fig. S19†), and the lowest free energy for each structure is given in Fig. 4. From Fig. 4 it can be found that the single-metal LDH of  $\text{Ni}(\text{OH})_2$  and  $\text{FeO}(\text{OH})$  have the largest  $\Delta G_{\text{H}^*}$  of over 0.60 eV. After doping with Fe, the  $\Delta G_{\text{H}^*}$  of the mixed-metal  $\text{NiFeO}(\text{OH})_3$  is reduced to 0.49 eV. By compositing with  $\text{Ni}_2\text{P}$ , all the  $|\Delta G_{\text{H}^*}|$  values of the LDH species can be greatly decreased, which is consistent with our experimental results, demonstrating the formation of a heterostructure of LDH and that  $\text{Ni}_2\text{P}$  can really boost the hydrogen evolution activity. Among them, the mixed-metal heterostructure of  $\text{Ni}_2\text{P}@\text{NiFeO}(\text{OH})_3$  exhibits the lowest  $\Delta G_{\text{H}^*}$  value of 0.06 eV at the catalytic site of Ni (Fig. S19†), being closer to the ideal value of zero. Thus, it shows that the highest HER performance benefits from the synergistic electron effect after the formation of the  $\text{Ni}_2\text{P}@\text{NiFeO}(\text{OH})_3$  heterostructure.

### Electrocatalytic OER

Electrocatalytic performance of the  $\text{Ni}_2\text{P}@\text{FePO}_x$  catalyst for OER was also evaluated in 1.0 M KOH solution at a scan rate of  $5 \text{ mV s}^{-1}$ , and the results indicate that  $\text{Ni}_2\text{P}@\text{FePO}_x$  was also converted to  $\text{Ni}_2\text{P}@\text{NiFe}$  hydroxide (P-NiFe) during OER as a real electrocatalyst (see below). For comparison, the electrocatalytic performances of NiFe-LDH, P-Ni and commercial  $\text{IrO}_2$  coated on NF were also investigated under the same conditions. As shown in Fig. 5a, P-NiFe exhibits a much higher current density at a given potential of 1.45 V in comparison to those of other catalysts. To avoid the interference of  $\text{Ni}^{\text{III/II}}$  oxidation waves at approximately 1.4 V, CCE was used to determine the overpotentials for OER of these catalysts at a current density of  $10 \text{ mA cm}^{-2}$ . As shown in Fig. 5c, P-NiFe displays a stable overpotential of 205 mV at  $10 \text{ mA cm}^{-2}$  during a 25 h CCE. This value is much lower than those of NiFe-LDH (250 mV), P-Ni (290 mV) and  $\text{IrO}_2$  (320 mV), indicating that the OER catalytic activity is also enhanced after the formation of a P-NiFe heterostructure. In addition, the Tafel slope of P-NiFe ( $32 \text{ mV dec}^{-1}$ ) is smaller than those of NiFe-LDH ( $70 \text{ mV dec}^{-1}$ ), P-Ni ( $105 \text{ mV dec}^{-1}$ ) and  $\text{IrO}_2$  ( $230 \text{ mV dec}^{-1}$ , see Fig. 5b), indicating its fast



Fig. 4 Free energy of  $\text{H}^*$  adsorption on different catalysts by DFT calculations.



Fig. 5 (a) IR-corrected LSV curves, with a scan rate of  $5 \text{ mV s}^{-1}$ . (b) Tafel plots for OER in 1.0 M KOH and (c) current density traces of CCE at  $10 \text{ mA cm}^{-2}$  (as well as 100 and  $1000 \text{ mA cm}^{-2}$  for P-NiFe, dashed line). (d) LSV curves of P-NiFe before (black square) and after (red circle) CCE for OER at  $10 \text{ mA cm}^{-2}$  for 25 h. Catalysts: P-NiFe (black), NiFe-LDH (red), P-Ni (blue) and  $\text{IrO}_2$  (orange).

catalytic rate and favorable OER kinetics. The high stable catalytic performance of P-NiFe was further confirmed by the LSV measurements, in which the LSV curves before and after 25 h of CCE at  $10 \text{ mA cm}^{-2}$  are almost identical (Fig. 5d).

For commercial hydrogen production by electrocatalytic water splitting, the development of non-precious OER electrocatalysts that can work with long-term stability at large current densities and low overpotentials is highly desirable. For the P-NiFe electrocatalyst, it only requires very low OER overpotentials of 230 and 430 mV to achieve large current densities of 100 and  $1000 \text{ mA cm}^{-2}$ , respectively, and P-NiFe exhibits impressive robustness for at least 25 h during CCE at a large current density of  $1000 \text{ mA cm}^{-2}$  in 1.0 M KOH solution (Fig. 5c), which exhibits much better performance than NiFe-LDH, in which NiFe-LDH shows an overpotential of 550 mV to achieve a current density of  $1000 \text{ mA cm}^{-2}$ , with the overpotential increasing to 650 mV after 25 h of CCE (Fig. S20†). To our knowledge, these values are among the lowest overpotentials of reported OER electrocatalysts for the corresponding current densities (see Table S1†). It should be mentioned that bare NF shows much lower activity for OER than that of P-NiFe under the same conditions (Fig. S9b†), indicating that the high OER activity originates from the P-NiFe catalyst rather than from the NF.

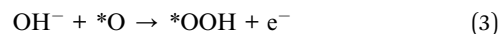
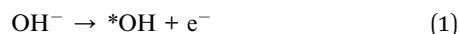
All the above results reveal that the OER catalytic activity of P-NiFe is also much enhanced compared to that of NiFe-LDH. In order to gain an in-depth understanding of the origin of the high catalytic activity of P-NiFe, a series of characterizations were performed on the P-NiFe catalyst after 25 h of CCE for OER. HRTEM (Fig. S21†) and elemental mapping images (Fig. S22†) indicate that the original amorphous iron phosphate in  $\text{Ni}_2\text{-P}@\text{FePO}_x$  also transformed into crystalline  $\text{Fe}(\text{OH})_3$  during CCE



in basic solution, while the Ni<sub>2</sub>P nanoparticles still exist in the heterostructure. These results are further confirmed by the XRD measurements, where the characteristic diffraction peaks of Ni<sub>2</sub>P and Fe(OH)<sub>3</sub> were all detected (Fig. S23†). However, the XPS results show the disappearance of the peaks of P and the low-energy peak of nickel (853.5 eV), as well as a shift toward higher binding energy for Ni (from 857.2 to 857.8 eV) in P-NiFe after CCE (Fig. S24†), indicating the surface oxidation of Ni<sub>2</sub>P to form nickel hydroxide during OER.<sup>8f,15a,15b</sup> The XPS patterns for the P-NiFe sample after the LSV measurement and before CCE (Fig. S25†) are similar to those after CCE, indicating that the surface oxidation of Ni<sub>2</sub>P into Ni(OH)<sub>2</sub> occurs rapidly during OER in solution. Furthermore, after the CCE, new peaks corresponding to the NiFe hydroxide appeared in the Raman spectroscopy of P-NiFe (Fig. S15†), while no obvious peaks were observed in the Raman spectroscopy of as-synthesized Ni<sub>2</sub>-P@FePO<sub>x</sub>. These observations indicate that the NiFe hydroxide formed on the surface of P-NiFe during the OER to serve as a real catalyst for OER,<sup>10b,13c,23</sup> which also acts as a protective layer to prevent the further corrosion of Ni<sub>2</sub>P.<sup>15a</sup>

Overall, the above results demonstrate that, during the CCE for OER, the as-prepared Ni<sub>2</sub>P@FePO<sub>x</sub> heterostructure was transformed into a new heterostructure comprised of NiFe hydroxide around the inner Ni<sub>2</sub>P nanoparticles. Such a transformation can be regarded as a self-optimization of Ni<sub>2</sub>-P@FePO<sub>x</sub> during the electrocatalytic process to form a more stable and more efficient catalyst of P-NiFe for OER. Similar to P-NiFe for HER, the inner Ni<sub>2</sub>P in P-NiFe for OER can also serve as a highly conductive, metallic support to provide a fast electron transfer pathway,<sup>13a,25</sup> and this was confirmed by the results of EIS measurements, in which P-NiFe shows a smaller charge transfer impedance than that of NiFe-LDH after 25 h of CCE for OER (Fig. S16b†). In addition, the results of ECSA measurements indicate that P-NiFe possesses 5-fold more active sites than NiFe-LDH (Fig. S17b†), which can be attributed to the extraction of Ni from NiFe-LDH and the increased surface roughness of P-NiFe after CCE (Fig. S26†), resulting in more active sites and enhanced OER activity.

To further understand the origin of the enhanced OER activity of the P-NiFe, DFT calculations were performed. The results of previous DFT calculations have already demonstrated that the OER activity of WOCs based on transition metal materials is mainly driven by the energetics of the OER intermediates (\*OH, \*O, and \*OOH, \* being the adsorption site) on the catalyst surfaces, and the adsorption energy difference between O and OH is the main descriptor that affects the trends in OER activity among these materials.<sup>9c</sup> In this context, we investigated seven model structures to simulate the overpotentials for oxygen evolution on the surfaces of Ni<sub>2</sub>P, Ni(OH)<sub>2</sub>, FeO(OH), Ni<sub>2</sub>P@Ni(OH)<sub>2</sub>, Ni<sub>2</sub>P@FeO(OH), NiFeO(OH)<sub>3</sub> (corresponding to NiFe-LDH), and Ni<sub>2</sub>P@NiFeO(OH)<sub>3</sub> (corresponding to P-NiFe), respectively, on the basis of the following OER mechanism:<sup>8f,17a,26</sup>



$$\eta = \max \{ \Delta G_1, \Delta G_2, \Delta G_3, \Delta G_4 \} / e - 1.23 \text{ V} \quad (5)$$

The free energies of the reactions (1) to (4) are denoted as  $\Delta G_1$  to  $\Delta G_4$ , respectively, and the overpotential  $\eta$  is defined in eqn (5). As is known, the rate-limiting step during OER for a given catalyst is the step with maximum  $\Delta G$  value among  $\Delta G_1$  to  $\Delta G_4$ , the lower rate-limiting energy barrier will lead to the smaller overpotential  $\eta$  (eqn (5)) and subsequently lead to higher OER activity.

The optimized structures of the intermediates in the free-energy landscape are shown in Fig. S27.† From Fig. S27† it can be found that Ni<sub>2</sub>P@NiFeO(OH)<sub>3</sub> displays the lowest rate-limiting energy barrier of 1.722 eV ( $\Delta G_1$ ), with the smallest calculated  $\eta$  value of 0.49 V. For Ni<sub>2</sub>P, the calculated results show that the rate-limiting step is the formation of \*OOH (reaction (3)) in an ideal Ni<sub>2</sub>P surface, with a very large overpotential ( $\eta = 1.08$  V), due to its largest binding energy of O as well as the relatively smaller binding energy of OOH (Fig. 6a), and the larger binding energies of Ni<sub>2</sub>P towards OH and O may be attributed to the metallic nature of Ni. For the surface-oxidized Ni<sub>2</sub>P@Ni(OH)<sub>2</sub> heterostructure, the rate-limiting step is the formation of \*O (reaction (2)), with a smaller  $\eta$  value of 0.62 V compared to that of pure Ni(OH)<sub>2</sub> ( $\eta = 0.80$  V), this is because the relatively smaller binding energy of O on Ni(OH)<sub>2</sub> has remarkably increased after combining with inner Ni<sub>2</sub>P in the Ni<sub>2</sub>P@Ni(OH)<sub>2</sub> heterostructure (see Fig. S27†), as Ni<sub>2</sub>P possesses the largest binding energies towards O (Fig. 6a), which is favorable for reaction (2), and consequently improves the energetics for OER.<sup>9c</sup> For the bimetal systems of NiFeO(OH)<sub>3</sub> and Ni<sub>2</sub>P@NiFeO(OH)<sub>3</sub>, the preferential active sites are Ni rather than Fe, as the binding energies of Fe to the OER intermediates (\*OH, \*O, and \*OOH) are too strong to the disadvantage of the desorption (Fig. 6a). Nevertheless, the binding energy of O and OOH on the Fe-doped NiFeO(OH)<sub>3</sub> can also be enhanced compared to the pure Ni(OH)<sub>2</sub> and result in higher OER activity, being similar to that of the Ni<sub>2</sub>P@Ni(OH)<sub>2</sub> heterostructure. More interestingly, after introducing both the heterostructure and Fe doping, the binding energies of OH and O on the Ni<sub>2</sub>P@NiFeO(OH)<sub>3</sub> with Ni active sites are further optimized to get the lowest rate-limiting energy barrier of 1.722 eV (Fig. S27†), with the smallest calculated  $\eta$  value of 0.49 V compared with those of NiFeO(OH)<sub>3</sub> ( $\eta = 0.59$  V) and the hypothetical Fe-covered Ni<sub>2</sub>P@FeO(OH) system ( $\eta = 0.73$  V). Interestingly, if  $\Delta E_{\text{OH}} - \Delta E_{\text{O}}$  (the difference in binding energy between OH and O) is adopted as the descriptor, a volcano-shaped plot containing the calculated overpotential *versus* ( $\Delta E_{\text{OH}} - \Delta E_{\text{O}}$ ) can be established (Fig. 6b), in which the overpotential of each model system follows the trend from our experiments, with the optimal ( $\Delta E_{\text{OH}} - \Delta E_{\text{O}}$ ) value around 0.4 eV. Undoubtedly, too low and too high values of ( $\Delta E_{\text{OH}} - \Delta E_{\text{O}}$ ) signify too strong binding energies of OH and O (or too weak binding energies of O and OH), being unfavorable to the formation of \*O and \*OH, respectively. Actually, the mixed-metal





Fig. 6 (a) Calculated binding energies of the OER intermediates, and (b) volcano-shaped plot of calculated overpotential versus the differences in binding energies between OH and O on the simulated surfaces of different catalysts.  $\text{NiFeO}(\text{OH})_3\text{-Ni}$  and  $\text{Ni}_2\text{P}@ \text{NiFeO}(\text{OH})_3\text{-Ni}$  represent the catalytic active sites for Ni, while  $\text{NiFeO}(\text{OH})_3\text{-Fe}$  and  $\text{Ni}_2\text{P}@ \text{NiFeO}(\text{OH})_3\text{-Fe}$  represent the catalytic active sites for Fe.

$\text{Ni}_2\text{P}@ \text{NiFeO}(\text{OH})_3$  heterostructure is located closer to the volcano summit, revealing that the heterostructure as well as the Fe-incorporation can effectively modulate the binding energies of the intermediates towards optimal values for enhancing its catalytic performance for OER.

### Electrocatalytic overall water splitting

Based on the above results, it can be seen that P-NiFe exhibits high electrocatalytic efficiency for both HER and OER. Accordingly, two P-NiFe-based NF electrodes were utilized to construct an electrolyzer for overall water splitting. The LSV and CCE measurements indicate that it only requires a cell voltage of 1.51 V to afford a  $10 \text{ mA cm}^{-2}$  current density in 1.0 M KOH aqueous solution (Fig. 7). This performance for overall water splitting is better than those of commercial benchmarks of  $\text{IrO}_2$  and Pt/C on NF (1.58 V) and NiFe-LDH on NF (1.72 V). The value of 1.58 V at  $10 \text{ mA cm}^{-2}$  for an electrolyzer consisting of  $\text{IrO}_2$  and Pt/C is in agreement with the reported value,<sup>3b,4a,10a,10b</sup> which validates our electrochemical measurement. To our knowledge, the facilely prepared, earth-abundant P-NiFe electrocatalyst exhibits the best catalytic performance for overall water splitting among the reported non-noble electrocatalysts



Fig. 7 (a) LSV curves of P-NiFe (black) and NiFe-LDH (red) as HER and OER bifunctional catalysts in 1.0 M KOH solution for overall water splitting.  $\text{IrO}_2$  and Pt/C as OER and HER benchmarks were measured for comparison (blue). (b) Current density traces of CCE at  $10 \text{ mA cm}^{-2}$  for overall water splitting in 1.0 M KOH for P-NiFe (black), NiFe-LDH (red), and commercial benchmarks of  $\text{IrO}_2$  and 20% Pt/C (blue).

(including those on nickel foam substrates) in basic electrolyte (Table S2†). In addition, as shown in Fig. 7b, the P-NiFe-based electrolyzer also exhibits remarkable stability, with negligible deactivation within 100 h of CCE at  $10 \text{ mA cm}^{-2}$ , and no significant change was observed in the LSV curves for overall water splitting before and after CCE (Fig. S28†). Moreover, the Faraday efficiency of the electrolyzer for overall water splitting at  $10 \text{ mA cm}^{-2}$  within 1 h was determined to be  $97 \pm 5\%$  ( $93.1 \pm 4.5 \mu\text{mol}$ ) for  $\text{H}_2$  and  $99 \pm 5\%$  ( $46.6 \pm 2.3 \mu\text{mol}$ ) for  $\text{O}_2$ , respectively, confirming the high electrocatalytic stability and efficiency of P-NiFe nanosheets. Furthermore, the above established electrolyzer could continuously release  $\text{H}_2$  and  $\text{O}_2$  bubbles with a single-cell AAA battery of 1.5 V (see video in the ESI†).

## Conclusion

Our studies have revealed that the nickel element in NiFe-LDH can be selectively phosphorized and extracted into  $\text{Ni}_2\text{P}$  nanoparticles to generate an  $\text{Ni}_2\text{P}@ \text{FePO}_x$  heterostructure, which is further transformed into a new heterostructure of P-NiFe comprised of NiFe hydroxide around the inner  $\text{Ni}_2\text{P}$  nanoparticles through a self-optimization of the  $\text{Ni}_2\text{P}@ \text{FePO}_x$  during the electrocatalytic process. The *in situ* formed P-NiFe electrocatalyst exhibits high electrocatalytic activity and stability for both HER and OER in 1.0 M KOH, and can be used as a bifunctional electrocatalyst for overall water-splitting, with a cell voltage of only 1.51 V at a current density of  $10 \text{ mA cm}^{-2}$ . Its electrocatalytic activity is among the most active earth-abundant bifunctional electrocatalysts reported to date, and is





even superior to the state-of-the-art noble-metal coupled electrocatalysts of IrO<sub>2</sub> and Pt/C on NF (1.58 V at 10 mA cm<sup>-2</sup>). The results of theoretical calculations suggest that the *in situ* formed P-NiFe heterostructure could optimize the adsorption energies for both HER and OER intermediates, thus dramatically enhancing its electrocatalytic activity. This facile and efficient strategy will open up new avenues for the construction of high-performance and low-cost electrocatalysts for overall water splitting to store intermittent solar energy and wind energy sources into hydrogen fuel.

## Conflicts of interest

There are no conflicts to declare.

## Acknowledgements

This work was supported by the NSFC (21331007, 21790052 and 21671032), the 973 Project of China (2014CB845602), the NSF of Guangdong Province (S2012030006240), and the National Postdoctoral Program for Innovative Talents (BX201600195).

## Notes and references

- (a) Y.-N. Gong, T. Ouyang, C.-T. He and T.-B. Lu, *Chem. Sci.*, 2016, **7**, 1070–1075; (b) Z. Lai, Y. Chen, C. Tan, X. Zhang and H. Zhang, *Chem.*, 2016, **1**, 59–77; (c) C. Tan, X. Cao, X. J. Wu, Q. He, J. Yang, X. Zhang, J. Chen, W. Zhao, S. Han, G. H. Nam, M. Sindoro and H. Zhang, *Chem. Rev.*, 2017, **117**, 6225–6331.
- (a) J.-W. Wang, P. Sahoo and T.-B. Lu, *ACS Catal.*, 2016, **6**, 5062–5068; (b) H. Yan, C. Tian, L. Wang, A. Wu, M. Meng, L. Zhao and H. Fu, *Angew. Chem., Int. Ed.*, 2015, **54**, 6325–6329; (c) Y. Jiao, Y. Zheng, K. Davey and S.-Z. Qiao, *Nat. Energy*, 2016, **1**, 16130; (d) Y. Liu, Q. Li, R. Si, G. D. Li, W. Li, D. P. Liu, D. Wang, L. Sun, Y. Zhang and X. Zou, *Adv. Mater.*, 2017, **29**, 1606200; (e) X. Zou and Y. Zhang, *Chem. Soc. Rev.*, 2015, **44**, 5148–5180.
- (a) M. Zhang, M. T. Zhang, C. Hou, Z. F. Ke and T. B. Lu, *Angew. Chem., Int. Ed.*, 2014, **53**, 13042–13048; (b) Y. Jin, H. Wang, J. Li, X. Yue, Y. Han, P. K. Shen and Y. Cui, *Adv. Mater.*, 2016, **28**, 3785–3790; (c) R. Liu, Y. Wang, D. Liu, Y. Zou and S. Wang, *Adv. Mater.*, 2017, **29**, 1701546; (d) S. Dou, C.-L. Dong, Z. Hu, Y.-C. Huang, J.-I. Chen, L. Tao, D. Yan, D. Chen, S. Shen, S. Chou and S. Wang, *Adv. Funct. Mater.*, 2017, **27**, 1702546.
- (a) H. Wang, H. W. Lee, Y. Deng, Z. Lu, P. C. Hsu, Y. Liu, D. Lin and Y. Cui, *Nat. Commun.*, 2015, **6**, 7261; (b) P. Wang, X. Zhang, J. Zhang, S. Wan, S. Guo, G. Lu, J. Yao and X. Huang, *Nat. Commun.*, 2017, **8**, 14580.
- (a) C. G. Morales-Guio and X. Hu, *Acc. Chem. Res.*, 2014, **47**, 2671–2681; (b) M. R. Gao, J. X. Liang, Y. R. Zheng, Y. F. Xu, J. Jiang, Q. Gao, J. Li and S. H. Yu, *Nat. Commun.*, 2015, **6**, 5982; (c) X. Long, G. Li, Z. Wang, H. Zhu, T. Zhang, S. Xiao, W. Guo and S. Yang, *J. Am. Chem. Soc.*, 2015, **137**, 11900–11903; (d) X. Y. Yu, Y. Feng, Y. Jeon, B. Guan, X. W. Lou and U. Paik, *Adv. Mater.*, 2016, **28**, 9006–9011.
- (a) Y. J. Tang, M. R. Gao, C. H. Liu, S. L. Li, H. L. Jiang, Y. Q. Lan, M. Han and S. H. Yu, *Angew. Chem., Int. Ed.*, 2015, **54**, 12928–12932; (b) J. S. Li, Y. Wang, C. H. Liu, S. L. Li, Y. G. Wang, L. Z. Dong, Z. H. Dai, Y. F. Li and Y. Q. Lan, *Nat. Commun.*, 2016, **7**, 11204.
- F. Wang, Y. Li, T. A. Shifa, K. Liu, F. Wang, Z. Wang, P. Xu, Q. Wang and J. He, *Angew. Chem., Int. Ed.*, 2016, **55**, 6919–6924.
- (a) A. B. Laursen, K. R. Patraju, M. J. Whitaker, M. Retuerto, T. Sarkar, N. Yao, K. V. Ramanujachary, M. Greenblatt and G. C. Dismukes, *Energy Environ. Sci.*, 2015, **8**, 1027–1034; (b) Y. Shi and B. Zhang, *Chem. Soc. Rev.*, 2016, **45**, 1529–1541; (c) J. F. Callejas, C. G. Read, C. W. Roske, N. S. Lewis and R. E. Schaak, *Chem. Mater.*, 2016, **28**, 6017–6044; (d) E. J. Popczun, J. R. McKone, C. G. Read, A. J. Biacchi, A. M. Wiltrout, N. S. Lewis and R. E. Schaak, *J. Am. Chem. Soc.*, 2013, **135**, 9267–9270; (e) X. Wang, W. Li, D. Xiong, D. Y. Petrovykh and L. Liu, *Adv. Funct. Mater.*, 2016, **26**, 4067–4077; (f) B. You, N. Jiang, M. L. Sheng, M. W. Bhushan and Y. J. Sun, *ACS Catal.*, 2016, **6**, 714–721; (g) D. Y. Chung, S. W. Jun, G. Yoon, H. Kim, J. M. Yoo, K. S. Lee, T. Kim, H. Shin, A. K. Sinha, S. G. Kwon, K. Kang, T. Hyeon and Y. E. Sung, *J. Am. Chem. Soc.*, 2017, **139**, 6669–6674; (h) C. Tang, R. Zhang, W. Lu, L. He, X. Jiang, A. M. Asiri and X. Sun, *Adv. Mater.*, 2017, **29**, 1602441; (i) X. Xiao, C.-T. He, S. Zhao, J. Li, W. Lin, Z. Yuan, Q. Zhang, S. Wang, L. Dai and D. Yu, *Energy Environ. Sci.*, 2017, **10**, 893–899.
- (a) M. Gong and H. Dai, *Nano Res.*, 2014, **8**, 23–39; (b) Y. Liang, Y. Li, H. Wang, J. Zhou, J. Wang, T. Regier and H. Dai, *Nat. Mater.*, 2011, **10**, 780–786; (c) B. Zhang, X. Zheng, O. Voznyy, R. Comin, M. Bajdich, M. Garcia-Melchor, L. Han, J. Xu, M. Liu, L. Zheng, F. P. Garcia de Arquer, C. T. Dinh, F. Fan, M. Yuan, E. Yassitepe, N. Chen, T. Regier, P. Liu, Y. Li, P. De Luna, A. Janmohamed, H. L. Xin, H. Yang, A. Vojvodic and E. H. Sargent, *Science*, 2016, **352**, 333–337.
- (a) N. Jiang, B. You, M. Sheng and Y. Sun, *Angew. Chem., Int. Ed.*, 2015, **54**, 6251–6254; (b) C. Tang, N. Cheng, Z. Pu, W. Xing and X. Sun, *Angew. Chem., Int. Ed.*, 2015, **54**, 9351–9355; (c) J. Duan, S. Chen, A. Vasiliev and S. Z. Qiao, *ACS Nano*, 2016, **10**, 8738–8745; (d) L. Jiao, Y.-X. Zhou and H.-L. Jiang, *Chem. Sci.*, 2016, **7**, 1690–1695; (e) Y. Jia, L. Zhang, G. Gao, H. Chen, B. Wang, J. Zhou, M. T. Soo, M. Hong, X. Yan, G. Qian, J. Zou, A. Du and X. Yao, *Adv. Mater.*, 2017, **29**, 1700017.
- (a) J. Bao, X. Zhang, B. Fan, J. Zhang, M. Zhou, W. Yang, X. Hu, H. Wang, B. Pan and Y. Xie, *Angew. Chem., Int. Ed.*, 2015, **54**, 7399–7404; (b) H. Hu, B. Guan, B. Xia and X. W. Lou, *J. Am. Chem. Soc.*, 2015, **137**, 5590–5595; (c) J. X. Feng, H. Xu, Y. T. Dong, S. H. Ye, Y. X. Tong and G. R. Li, *Angew. Chem., Int. Ed.*, 2016, **55**, 3694–3698; (d) J. Ping, Y. Wang, Q. Lu, B. Chen, J. Chen, Y. Huang, Q. Ma, C. Tan, J. Yang, X. Cao, Z. Wang, J. Wu, Y. Ying and H. Zhang, *Adv. Mater.*, 2016, **28**, 7640–7645; (e) X. Xu, C. Su, W. Zhou, Y. Zhu, Y. Chen and Z. Shao, *Adv. Sci.*, 2016, **3**, 1500187; (f) Y. Pi, Q. Shao, P. Wang, F. Lv, S. Guo,



- J. Guo and X. Huang, *Angew. Chem., Int. Ed.*, 2017, **56**, 4502–4506; (g) D. A. Corrigan, *J. Electrochem. Soc.*, 1987, **134**, 377.
- 12 (a) M. Gong, Y. Li, H. Wang, Y. Liang, J. Z. Wu, J. Zhou, J. Wang, T. Regier, F. Wei and H. Dai, *J. Am. Chem. Soc.*, 2013, **135**, 8452–8455; (b) J. Luo, J. H. Im, M. T. Mayer, M. Schreier, M. K. Nazeeruddin, N. G. Park, S. D. Tilley, H. J. Fan and M. Gratzel, *Science*, 2014, **345**, 1593–1596; (c) X. Lu and C. Zhao, *Nat. Commun.*, 2015, **6**, 6616; (d) J. Qi, W. Zhang, R. Xiang, K. Liu, H. Y. Wang, M. Chen, Y. Han and R. Cao, *Adv. Sci.*, 2015, **2**, 1500199; (e) X. L. Zhu, C. Tang, H. F. Wang, Q. Zhang, C. H. Yang and F. Wei, *J. Mater. Chem. A*, 2015, **3**, 24540–24546; (f) F. Dionigi and P. Strasser, *Adv. Energy Mater.*, 2016, **6**, 1600621; (g) C. N. Chervin, P. A. DeSario, J. F. Parker, E. S. Nelson, B. W. Miller, D. R. Rolison and J. W. Long, *ChemElectroChem*, 2016, **3**, 1369–1375; (h) M. Gorlin, J. Ferreira de Araujo, H. Schmies, D. Bernsmeier, S. Drespe, M. Gliech, Z. Jusys, P. Chernev, R. Kraehnert, H. Dau and P. Strasser, *J. Am. Chem. Soc.*, 2017, **139**, 2070–2082.
- 13 (a) H. Liang, A. N. Gandi, D. H. Anjum, X. Wang, U. Schwingenschlogl and H. N. Alshareef, *Nano Lett.*, 2016, **16**, 7718–7725; (b) Y. Yan, B. Y. Xia, X. Ge, Z. Liu, A. Fisher and X. Wang, *Chem.–Eur. J.*, 2015, **21**, 18062–18067; (c) B. Konkena, J. Masa, A. J. R. Botz, I. Sinev, W. Xia, J. Koßmann, R. Drautz, M. Muhler and W. Schuhmann, *ACS Catal.*, 2017, **7**, 229–237.
- 14 C. Y. Son, I. H. Kwak, Y. R. Lim and J. Park, *Chem. Commun.*, 2016, **52**, 2819–2822.
- 15 (a) M. Ledendecker, S. Krick Calderon, C. Papp, H. P. Steinruck, M. Antonietti and M. Shalom, *Angew. Chem., Int. Ed.*, 2015, **54**, 12361–12365; (b) G.-F. Chen, T. Y. Ma, Z.-Q. Liu, N. Li, Y.-Z. Su, K. Davey and S.-Z. Qiao, *Adv. Funct. Mater.*, 2016, **26**, 3314–3323; (c) D. Li, H. Baydoun, C. N. Verani and S. L. Brock, *J. Am. Chem. Soc.*, 2016, **138**, 4006–4009.
- 16 (a) J. Rossmeisl, Z. W. Qu, H. Zhu, G. J. Kroes and J. K. Nørskov, *J. Electroanal. Chem.*, 2007, **607**, 83–89; (b) R. V. Mom, J. Cheng, M. T. M. Koper and M. Sprik, *J. Phys. Chem. C*, 2014, **118**, 4095–4102.
- 17 (a) Y. T. Xu, X. Xiao, Z. M. Ye, S. Zhao, R. Shen, C. T. He, J. P. Zhang, Y. Li and X. M. Chen, *J. Am. Chem. Soc.*, 2017, **139**, 5285–5288; (b) J. K. Nørskov, T. Bligaard, A. Logadottir, J. R. Kitchin, J. G. Chen, S. Pandelov and U. Stimming, *J. Electrochem. Soc.*, 2005, **152**, J23.
- 18 (a) O. Diaz-Morales, I. Ledezma-Yanez, M. T. M. Koper and F. Calle-Vallejo, *ACS Catal.*, 2015, **5**, 5380–5387; (b) M. Bajdich, M. Garcia-Mota, A. Vojvodic, J. K. Nørskov and A. T. Bell, *J. Am. Chem. Soc.*, 2013, **135**, 13521–13530.
- 19 Q. Guan and W. Li, *J. Catal.*, 2010, **271**, 413–415.
- 20 Y. F. Xu, M. R. Gao, Y. R. Zheng, J. Jiang and S. H. Yu, *Angew. Chem., Int. Ed.*, 2013, **52**, 8546–8550.
- 21 Z. Hu, Z. Shen and J. C. Yu, *Chem. Mater.*, 2016, **28**, 564–572.
- 22 Y. Liu, H. Wang, D. Lin, C. Liu, P.-C. Hsu, W. Liu, W. Chen and Y. Cui, *Energy Environ. Sci.*, 2015, **8**, 1719–1724.
- 23 Y. Li and C. Zhao, *Chem. Mater.*, 2016, **28**, 5659–5666.
- 24 (a) J. Su, Y. Yang, G. Xia, J. Chen, P. Jiang and Q. Chen, *Nat. Commun.*, 2017, **8**, 14969; (b) P. Chen, K. Xu, S. Tao, T. Zhou, Y. Tong, H. Ding, L. Zhang, W. Chu, C. Wu and Y. Xie, *Adv. Mater.*, 2016, **28**, 7527–7532.
- 25 (a) P. Chen, K. Xu, Z. Fang, Y. Tong, J. Wu, X. Lu, X. Peng, H. Ding, C. Wu and Y. Xie, *Angew. Chem., Int. Ed.*, 2015, **54**, 14710–14714; (b) Y. Liu, C. Xiao, M. Lyu, Y. Lin, W. Cai, P. Huang, W. Tong, Y. Zou and Y. Xie, *Angew. Chem., Int. Ed.*, 2015, **54**, 11231–11235.
- 26 K. Fan, H. Chen, Y. Ji, H. Huang, P. M. Claesson, Q. Daniel, B. Philippe, H. Rensmo, F. Li, Y. Luo and L. Sun, *Nat. Commun.*, 2016, **7**, 11981.

